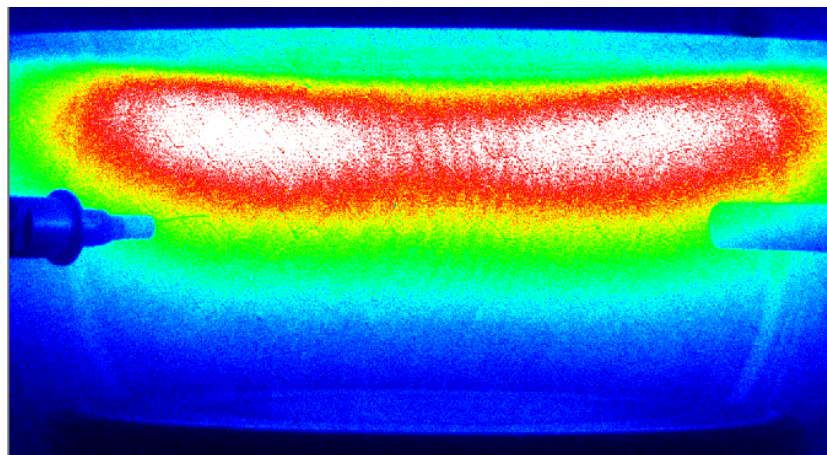**RUHR
UNIVERSITÄT
BOCHUM**

**RU**B

# Comparison of several techniques for obtaining the spatially resolved emissivity in low–temperature inductively coupled plasmas

Bericht zum SOWAS–Praktikum
im Masterstudiengang Physik
an der Ruhr-Universität Bochum

von

Philip Lucke
Marc Fehling

Bochum, Wintersemester 2014/2015

# Contents

# List of Figures

# Chapter 1

# Introduction

The plasma state is the most wide–spread naturally occurring state of the visible matter in the universe. Also artificially produced plasmas find broad application in many human activities. The plasma is characterized by a set of parameters, like e.g. charged–particle densities and temperatures. Naturally these parameters cover quite broad ranges in values. The measurements of these parameters is then highly desirable and a number of diagnostics have been developed for the task. One of the most well–known ones are the Langmuir probes and the optical emission spectroscopy.

Depending on the conditions the plasmas can be also quite inhomogeneous, meaning that one or more of its characteristics vary in space. This is especially true for elevated pressures and molecular gases. The different diagnostic techniques are differently suited to deal with this challenge. Some, like e.g. the Langmuir probe, can provide spatially resolved information, others like the optical emission spectroscopy deliver only line–averaged results.

The presented investigations apply these techniques — a Langmuir probe and two implementations of emission measurements — to obtain the local emissivity spatially resolved in a low–temperature inductively coupled plasma (ICP) operated in hydrogen. Particularly, an optical probe developed in the local institute for experimental physics V (EPV), a standard Langmuir probe and an Abel inversion method applied on ICCD camera images are used. The Langmuir probe actually delivers information about the electron energy distribution function (EEDF) which can be used to calculate the local excitation rate. The probe measurements provide simultaneously information on several other plasma characteristics, which are also presented for completeness. This report is basically a reproduction of the measurements presented in Du et al. [DCLC10].
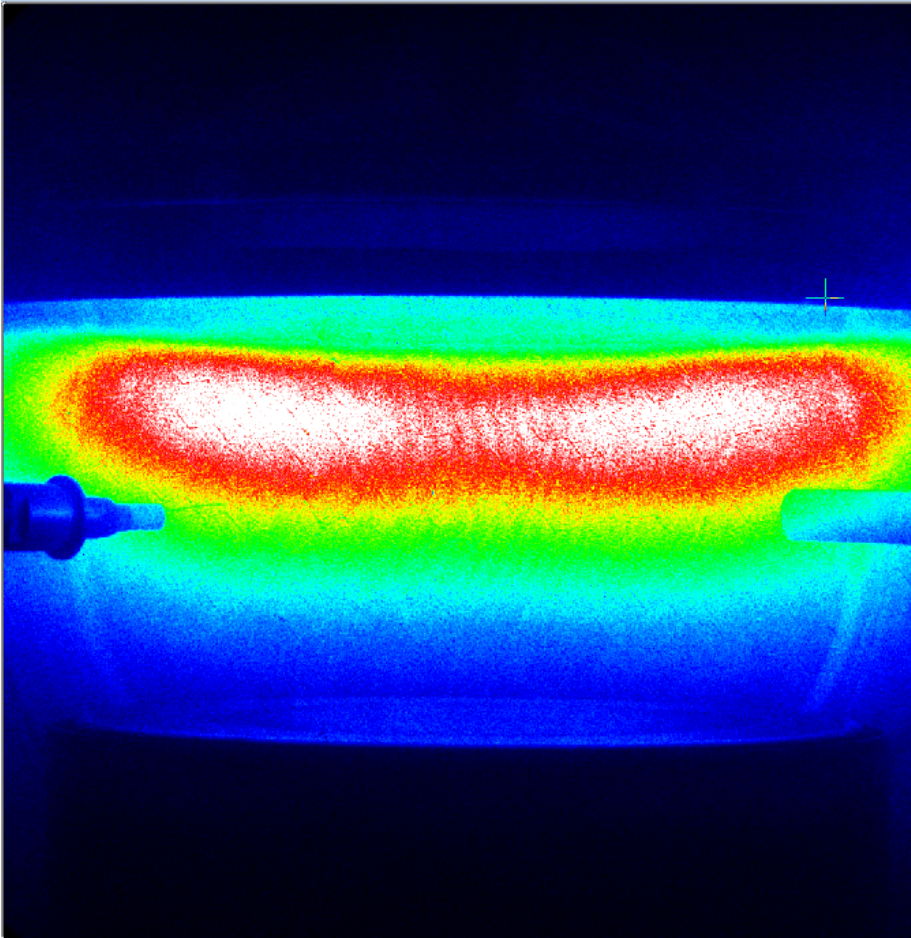
Figure 1.1: ICCD camera photograph of the ICP discharge with both optical probe (right) and Langmuir probe (left) moved in. In a way this figure shows all three diagnostics applied.

# Chapter 2

# Setup

In this experiment a modified GEC cell [DCLC10] is used as displayed in Fig. 2.1. The investigations were performed in the laboratories of the EPV institute. The chamber has a diameter of 25 cm, the upper quartz dome housing the RF antenna and the lower plate are 12 cm and 10 cm wide, respectively, and their distance is approximately 5 cm.

The optical and the Langmuir probe are inserted in the plasma from two different side ports while the ICCD camera takes pictures through a big flange as shown in Fig. 2.1(b). Both probes are operating in the plane midway between quartz dome and plate and are movable in radial direction with stepper motors. The ICCD camera is mounted on an optical bank which allows its whole setup to be moved.

Hydrogen is used as the discharge gas. The ICP discharge is running in H–mode with a constant supplied power of 300 W at pressures of 3 Pa, 10 Pa and 20 Pa. For the measurements the intensity of the $H_\alpha$–line is used. In the ICCD measurements it is isolated from the rest of the plasma emission by using an interference filter. In the measurements with the optical probe a spectrometer is used. For the radial measurements with the probes the center of the chamber is chosen to be the origin in the horizontal direction. Probe measurements start at the chamber wall for which optical and Langmuir probe need to be moved in 1.5 cm and 0.5 cm in this experiment, respectively. The hydrogen mass flow is generally set to 15 sccm, however for the 20 Pa measurement it needs to be increased to 30 sccm otherwise the desired pressure can not be achieved.



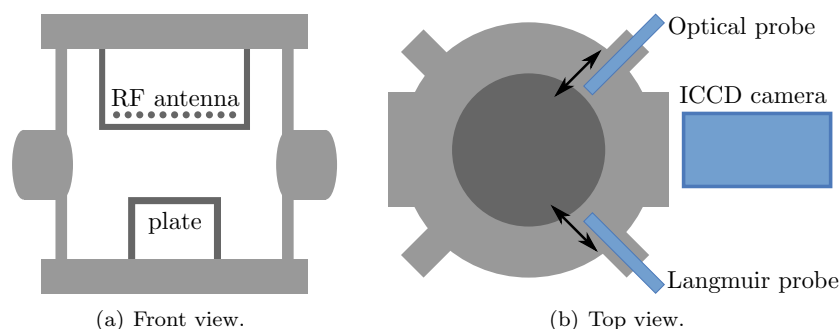(a) Front view.　　　　　　(b) Top view.

Figure 2.1: Sketches of the modified GEC cell used. [DCLC10, based on Fig. 8]

# Chapter 3
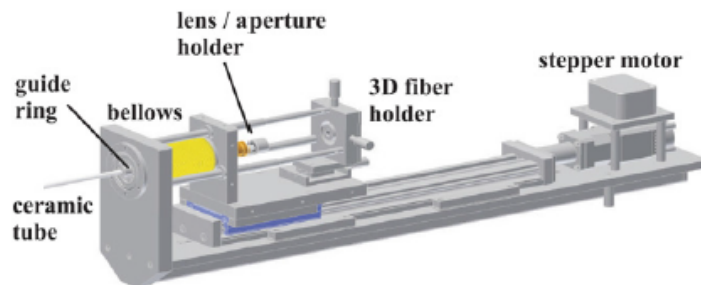
# Optical probe

## 3.1 Setup of the optical probe



Figure 3.1: The optical probe and its components. [DCLC10, Fig. 4]
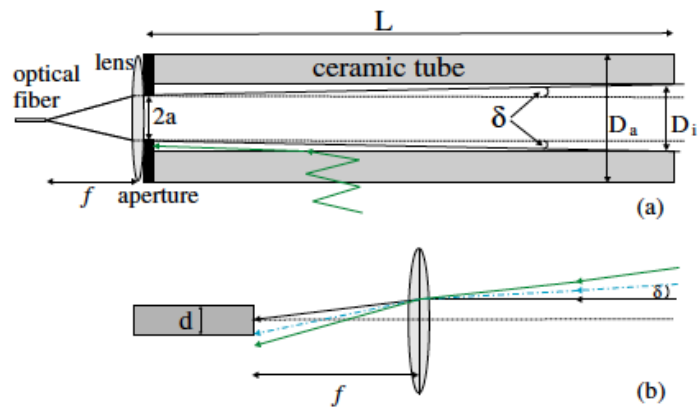


Figure 3.2: Schematic of the optical probe. (a) Setup of the probe. (b) Determination of the solid angle. [DCLC10, Fig. 2]

Fig. 3.1 shows the construction of the optical probe. A ceramic tube with an optical fiber attached to it is immersed in the plasma via a stepper motor. Fig. 3.2depicts the working principle of the optical probe. The ceramic tube of length $L$ is entered into the plasma where it collects the emission light of the plasma. At the end of the tube there is an aperture, so that just light within a very small solid angle is captured with the optical fiber and reflections from the tube are rejected. The light goes through a lens from the tube to the fiber. The solid angle is then given by:

$$\tan(\delta) = \frac{d/2}{f} \ ,$$
(3.1)

$\delta$ is the solid angle, $f$ the focal length of the lens and $d$ the diameter of the optical fiber.

## 3.2 Theory

Because the construction of the optical probe only allows collection of light within very small solid angles there exists a very simple connection between the detector signal $S(x)$ and the local emissivity $\varepsilon(x)$

$$S(x) = \int_x^{L_p} \varepsilon(x) dx \ ,$$
(3.2)

with $x$ the position of the probe and $L_p$ the diameter of the modified GEC cell. So the local emissivity is given by:

$$\varepsilon(x) = -\frac{dS(x)}{dx} \ .$$
(3.3)

## 3.3 Numerical approach

The optical probe is connected by an optical fiber with a spectrometer (Ocean Optics HR4000). The spectrometer allows the recording of the whole plasma spectrum from which the intensity of the $H_\alpha$–line at 656.28 nm is obtained. The spectrometer integrates the signal over a predefined time interval to increase the signal and to reduce the random noise. For the measurements at 3 Pa the integration time is 8 s, for 10 Pa it is 8 s and for 20 Pa it is 8 s. For each plasma condition the measurements at each position of the optical probe are repeated several times (8 measurements at 3 Pa and 4 for the 10 Pa and 20 Pa cases) and an averaged spectrum is obtained. These settings are chosen because for them the highest obtained intensity is just under the maximum value allowed for the

spectrometer. In the experiment the detector signal $S(x)$ is the intensity of the $H_\alpha$–line. To get the detector signal out of the experimental data one takes the data at each probe position and subtracts the background spectrum. Then one reads out the peak value of the $H_\alpha$–line. This peak value is always at the same position in the data for every probe position.

To obtain the emissivity the differentiation of the signal is done with the central difference quotient:

$$f'(x) = \frac{f(x+h) - f(x-h)}{2h} \quad .$$

Here $h$ is the differentiation step, equal to the distance between the consecutive measurement points. In these measurements it amounts to $0.5\,\text{cm}$. Fig. 3.3
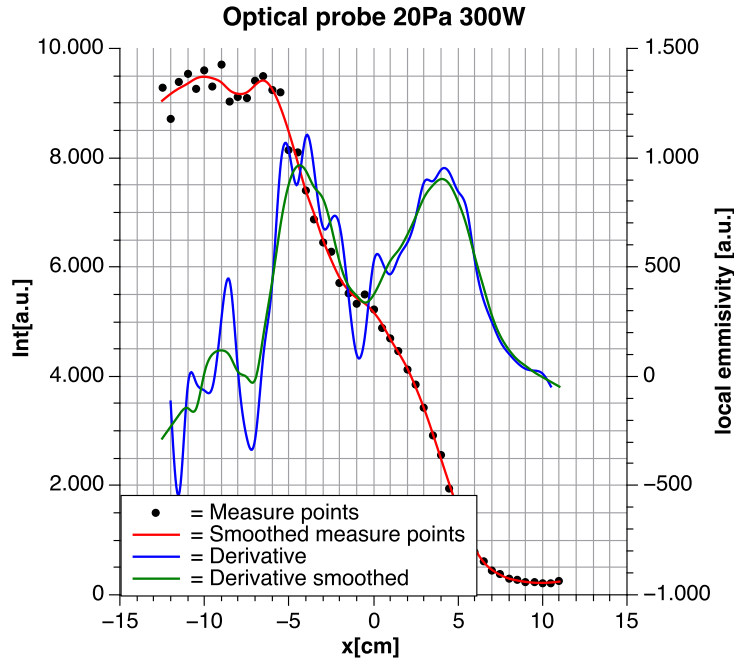


Figure 3.3: Probe position against detector signal and local emissivity.

shows the probe position on the $x$–axis against the recorded detector signal and the local emissivity, calculated from it as a function of the probe position. It is seen that a noise is present in the measured data, which is enhanced in the differentiation process. The obtained emissivity profiles are then too noisy and no definite features can be observed. Therefore one uses Savitzky–Golay smoothing to reduce the noise in the measurement. This is shown in the red curve. The green curve shows the differentiation of the smoothed data where a double peak structure can now be clearly identified.

### 3.3.1   Savitzky–Golay smoothing

Savitzky–Golay smoothing uses a polynomial least squares fit of $k^{th}$ degree to fit data of at least $k+1$ data points [SG64]. In the data analysis of this experiment one uses a polynomial of $2^{nd}$–degree through 7 data points

$$y = a_2(x - x_0)^2 + a_1(x - x_0) + a_0 \ . \tag{3.4}$$

The fit provides the polynomial coefficients $a_0 \ a_1 \ a_2$ for each window of 7 points around its central point at $x_0$. They are used to calculate the polynomial value at $x_0$ which is taken as the smoothed value at that point. The smoothed values for the first and the last three points are obtained with the coefficients of the first and last window, respectively.

A big advantage of the Savitzky–Golay smoothing is, that it is easy to obtain the derivatives of the smoothed data. Therefore the same smoothing algorithm is used also for the processing of the Langmuir probe data. The derivative of the data is given by the derivative of the fitting curve. The first derivative is given by:

$$f'(x) = 2a_2(x - x_0) + a_1 \ .$$

So the smoothed first derivative at $x_0$ is given by $a_1$. Only at the edges the whole polynomial must be taken into account. The second derivative is given by:

$$f''(x) = 2a_2 \ .$$

# Chapter 4

# Langmuir probe

## 4.1 Druyvesteyn formula

In the experiment one measures the probe current as a function of the probe voltage. The Druyvesteyn formula [Dru30] relates the electron energy probability function (EEPF) with the measured current–voltage curve:

$$\text{EEPF}(e(U_p - U)) = \frac{\sqrt{8m}}{e^{\frac{3}{2}} A_p} \frac{d^2 I}{dU^2} \ ,$$

(4.1)

with $m$ the electron mass, $e$ the elementary charge, $U_p$ the plasma potential, $A_p$ the probe surface area and $\frac{d^2 I}{dU^2}$ the second derivative of the probe current $I$ with respect to the probe voltage $U$. The electron energy distribution function (EEDF) is related to the EEPF by:

$$\text{EEDF}(e(U_p - U)) = \sqrt{E} \ \text{EEPF}(e(U_p - U)) \ .$$

(4.2)

The zero crossing of the smoothed measurement data shown in Fig. 4.1 yields the floating potential $(U_f)$. The inflection point i.e. the zero crossing of the second derivative gives the plasma potential $(U_p)$. In Fig. 4.1 no difference between the measurement data and the smoothed data can be seen. The differences are on a much smaller scale, but the smoothing is necessary because the noise increases when one differentiates the data especially when the data has to be differentiated twice.

## 4.2 Plasma parameters

From the measured EEDF the electron density and effective temperature can be obtained. The electron density $n_e$ is given by the zeroth moment of the EEDF:

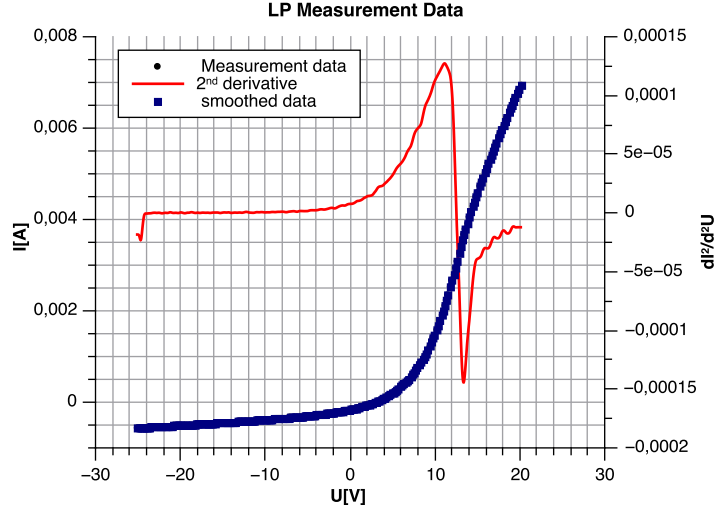$$n_e = \int_0^{E_{max}} EEDF dE$$

(4.3)

Figure 4.1: Probe voltage over probe current as a function of the probe voltage and second derivative.

The first moment of the EEDF yields the mean energy:

$$\langle E \rangle = \frac{\int_0^{E_{max}} E \; EEDF dE}{n_e} \; . \tag{4.4}$$

With the mean energy an effective temperature $T_{eff}$ can be calculated:

$$T_{eff} = \frac{2}{3}\langle E \rangle \; . \tag{4.5}$$

To obtain the local emissivity, it is assumed that the plasma is described by the corona model. This approximation is valid at low electron density and high electron temperature. Because of this the probability of de–excitation due to electron impact is negligibly small. So de–excitation happens only by spontaneous emission. The corona model assumes that upward transition only happens due to electron collision, while downward transition is only depending on radiative decay. This means that the local excitation rate is proportional to the local emission rate

$$n_e X_{1p}^{exc} = \frac{n_p}{n_1} A_p \tag{4.6}$$

with $X_{1p}^{exc}$ the excitation rate constant from the ground state to the excited state and $A_p$ the Einstein coefficient for radiative decay of the excited state. In this experiment one observes the H$\alpha$–line emission. So one needs the excitation from the ground state to the $p = 3$ state of the hydrogen atom. This excitation rate

is then proportional to the spontaneous emission of the H$\alpha$–line. The excitation rate constant $X$ can be calculated using the Arrhenius formula, which yields the Arrhenius form. With the Arrhenius formula the excitation rate depends on the effective temperature and thus on the mean energy of the electrons:

$$X = A(T_{eff}) \exp\left(-\frac{12.09}{T_{eff}}\right) \ . \tag{4.7}$$

Here 12.09 eV is the excitation energy of the $p{=}3$ state in Hydrogen and $A(T_{eff})$ is a weak function of the Temperature. In the following it is treated as a constant. One can calculate the excitation rate also from the excitation cross section for hydrogen and the measured EEDF. There the excitation rate is given by:

$$X \ n_e = \int_0^{E_{end}} EEDF\sigma(E) \ v(E)dE \ , \tag{4.8}$$

$\sigma(E)$ is the cross section for the excitation from the ground state to the third excited state.

## 4.3    Excitation cross section

For the cross section a theoretical expression from Janev et al. (2003) is used. The excitation from the ground state to the third excited state is given by:

$$\sigma\left(1s \to 3\right) = \frac{\sigma_0}{\Delta E \ x}\left(1 - \frac{1}{x}\right)^\alpha \left[A_0 \ln(x) + \sum_{j=1}^4 \frac{A_j}{x^{j-1}}\right] \ , \tag{4.9}$$

$\sigma_0 = 5.98$, $A_j$ and $\alpha$ are numerical coefficients given in Table 4.1, $\Delta E =12.09$ eV is the energy needed for excitation and $x$ is given by $\frac{E}{\Delta E}$. [JRS03]

Fig. 4.2 shows the cross section for some hydrogen excitations whereas Fig. 4.3 shows the calculated cross section that is used later on. For the calculation equation 4.9 and the values given in Table 1 have been used. A comparison with Fig. 4.2 shows that the curves are identical.

## 4.4    Numerical approach

For the smoothing and derivation one uses the same Savitzky–Golay algorithm that was shown in the last chapter. One then plots the second derivative for each probe position and determines by eye the plasma potential. The EEPF and EEDF are calculated with the Druyvesteyn formula.

Table 4.1: Numerical coefficients for excitation cross section $\sigma$. [JRS03, Tab. 2]

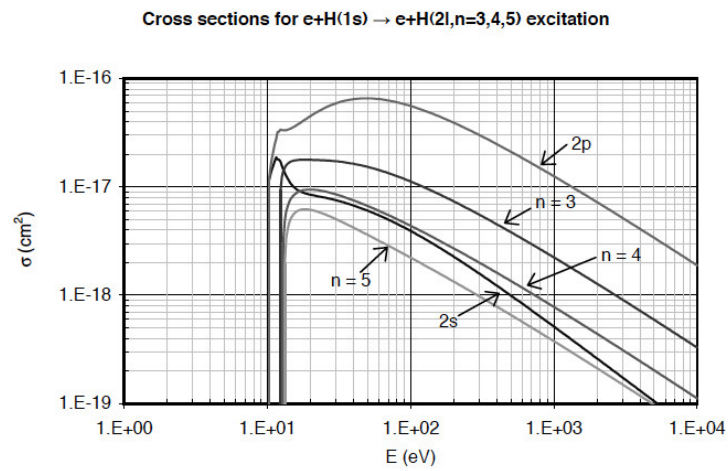| Transition | $1s \rightarrow n{=}3$ |
|---|---|
| $\alpha$ | 0.38277 |
| $A_0$ | 0.75448 |
| $A_1$ | 0.42956 |
| $A_2$ | -0.58288 |
| $A_3$ | 1.0693 |
| $A_4$ | 0.00 |



Figure 4.2: Excitation cross sections for various states of hydrogen. [JRS03]
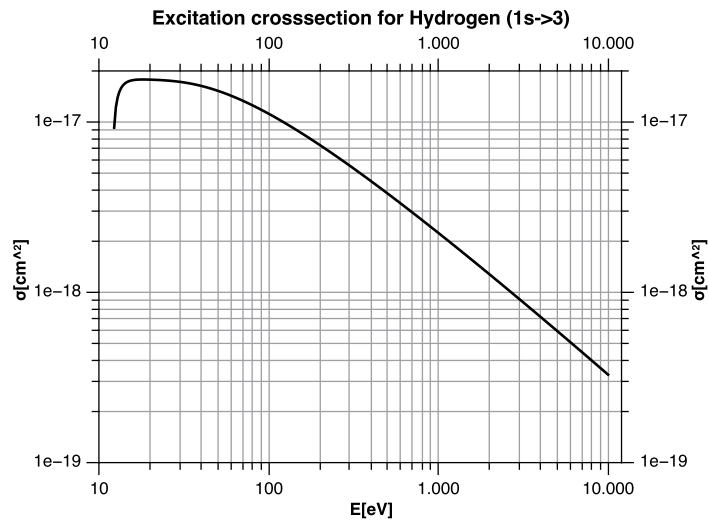


Figure 4.3: Theoretical excitation cross section for hydrogen.

With equations (4.3) and (4.5) the plasma parameters are calculated. All integrations are done with the Matlab *trapz* routine. The integration borders are given by the plasma potential and two times the difference between plasma potential and floating potential ($2(U_f - U_p)$).

One big problem was that the tails of the EEDFs and EEPFs are way too noisy but for the calculation of the excitation rate the tails play the biggest role. This was solved by assuming that the EEPF is of near Maxwellian form. Then the EEPF can be fitted with:

$$\text{EEPF} \propto A \exp(-\alpha(E - E_0)^b) \ . \tag{4.10}$$

The coefficient $A$ is given by $\text{EEPF}(E = E_0)$ with $E_0$ the energy with the highest probability where one finds the maximum of the EEPF. The other coefficient can be obtained with a polynomial least squares fit of first degree with the following form

$$\ln\left[\ln\left(\frac{A}{\text{EEPF}}\right)\right] = b \ln(E - E_0) + \ln(\alpha) \ ,$$

so that $b$ is given by the slope and $\alpha$ by the crossing with the $y$–axis.

For best agreement one has to fit each EEPF up to the highest possible energy. It is given by the highest energy where the fitting coefficients are real. For an energy higher than that they would become imaginary. So our algorithm consists of a while loop that starts the fit with an energy of $23\,\text{eV}$, checks if the coefficients are real or imaginary and if they are imaginary decreases the energy by $0.25\,\text{eV}$ and continues this procedure until they are real. Then the values of the coefficients and the energy up to which the fit is done are saved.

Fig. 4.4 shows the EEPF and the fitted EEPF for the probe position of -3.7 cm. As one can see the fit represents the data well.

Fig. 4.5 shows the fitting coefficients for each probe position. The EEPF would be Maxwellian if $b$ would be 1. This is the case for the edges and the center. For the rest it is between 1 and 1.5 showing that the EEPF is always close to Maxwellian.

The coefficient $\alpha$ is mirrored in regard to the shape to $b$. Fig. 4.6 shows the maximum energy values used for the fit at each probe position. One can see that similarly to the coefficients $\alpha$ and $b$ the values are symmetrical around the discharge axis at $x = 0\,\text{cm}$. This is related to the spatial variation of the effective electron temperature. As will be shown this leads to a similar variation in the emissivity.
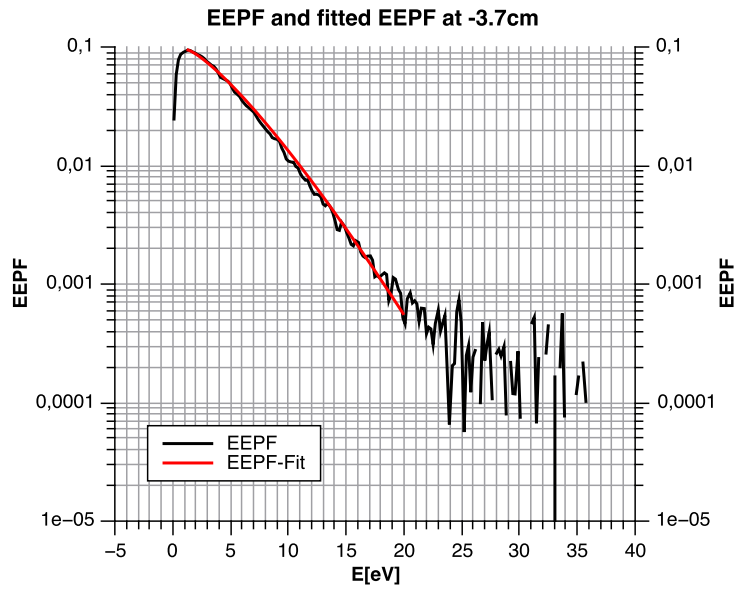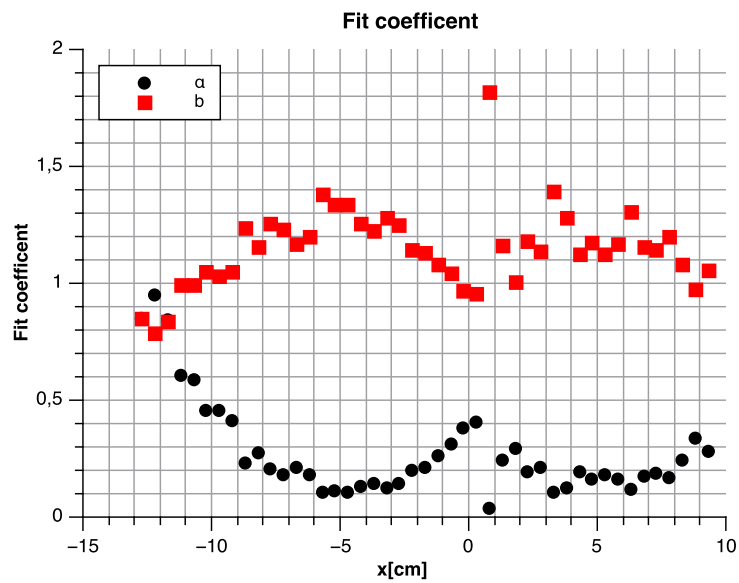
Figure 4.4: EEPF and fitted EEPF for 10 Pa.



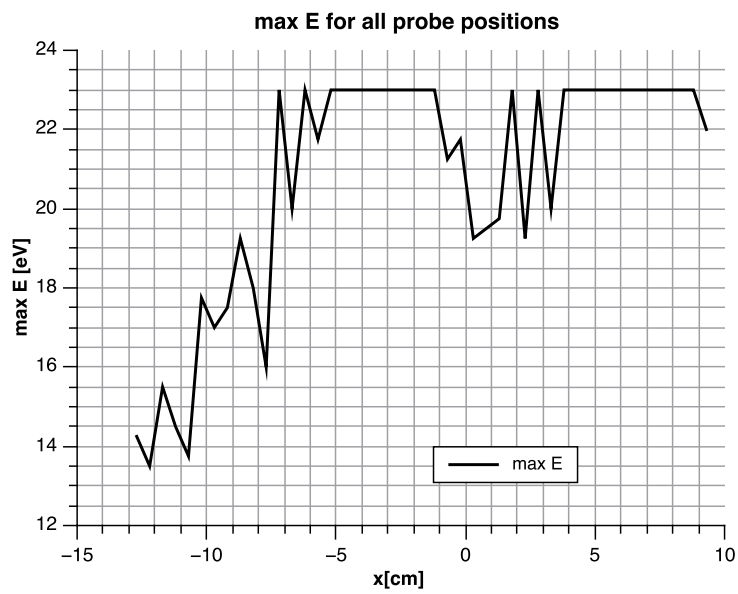Figure 4.5: Fitting coefficients over probe position for 10 Pa.

Figure 4.6: Maximum energy value over probe position for 10 Pa.

# Chapter 5

# Abel inversion

## 5.1 Physical background

The radiation of a plasma described by an emissivity $\epsilon$ can be recorded with optical instruments such as cameras, optical fibers etc. However detectors do not provide the emissivity itself but its line integration $h$ (see Fig. 5.1). Assuming axial symmetry of the emissivity this relation can be written as

$$h(y) = \int_{-\infty}^{\infty} \epsilon(r(x))\,\mathrm{d}x = 2\int_{0}^{\infty} \epsilon(r(x))\,\mathrm{d}x \ .$$

A basic substitution to cylindrical coordinates leads to the following expression which is known as the Abel transformation.

$$h(y) = 2\int_{y}^{\infty} \epsilon(r)\frac{r}{\sqrt{r^2 - y^2}}\,\mathrm{d}r \tag{5.1}$$

The inverse transformation is shortly called Abel inversion

$$\epsilon(r) = -\frac{1}{\pi}\int_{r}^{\infty} \frac{\mathrm{d}h(y)}{\mathrm{d}y}\frac{1}{\sqrt{y^2 - r^2}}\,\mathrm{d}y \tag{5.2}$$

and additionally requires that the line integrated emissivity $h$ drops down to zero faster than $\frac{1}{r}$. [Pre91]

## 5.2 Numerical Abel inversion algorithm

The application of the analytic Abel inversion (5.2) on the detector signal $h$ requires its derivation which would lead to high noise. So instead of using the above formula, different algorithms for Abel inversion have been developed in the literature.

To process the results of this experiment the Abel inversion method by Pretzler (1991) is used which was introduced by him as a "Fourier–method". Its
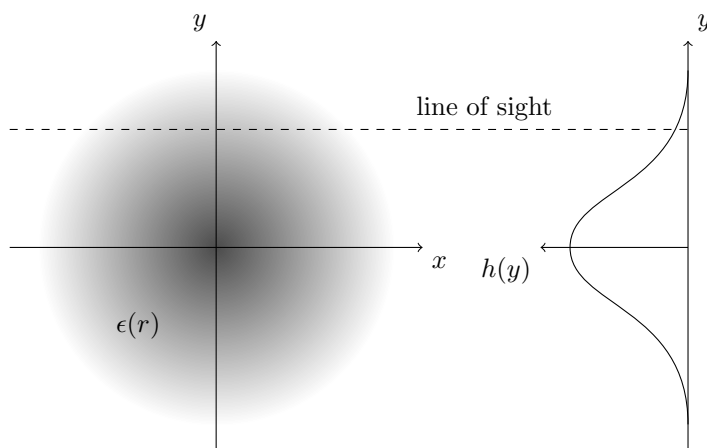
Figure 5.1: Geometric interpretation of a camera image of a radiating plasma. [Tho, based upon Abb1]

benefits, as advertised in the publication, are that no derivatives occur and no preparation of the measured data (e.g. smoothing) is necessary, but it requires the detector signal to vanish after a characteristic radius $r = R$. The method's basic concept is to present the emissivity $\epsilon$

$$\epsilon(r) = \sum_{n=N_l}^{N_u} A_n f_n(r) \tag{5.3}$$
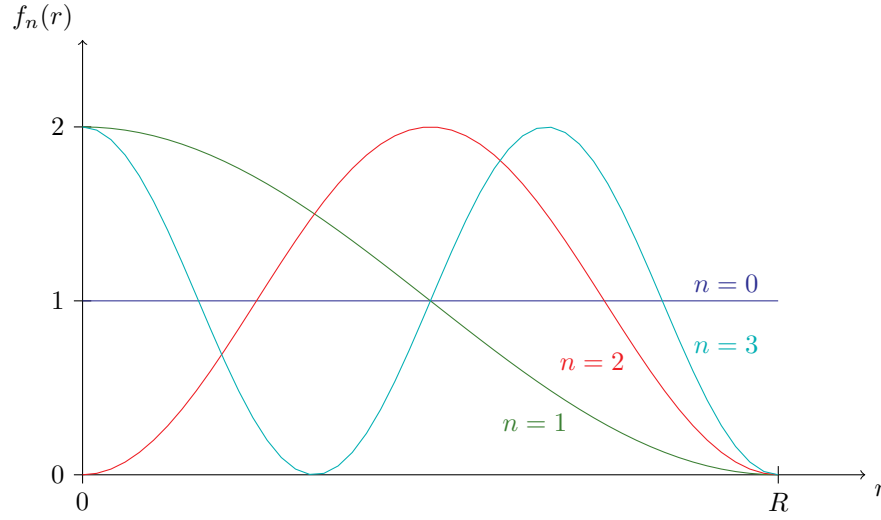
with a set of cosine functions $f_n$

$$f_n(r) = \begin{cases} 1 - (-1)^n \cos\left(n\pi \frac{r}{R}\right) & \text{for } n > 0 \\ 1 & \text{for } n = 0 \end{cases}$$

where the coefficients $A_n$ are constants and the parameters $N_l$ and $N_u$ describe the lower and upper limit of the expansion. Inserting the emissivity (5.3) in the Abel transformation (5.1) then yields

$$h(y) = 2 \sum_{n=N_l}^{N_u} A_n \underbrace{\int_y^R f_n(r) \frac{r}{\sqrt{r^2 - y^2}} \, \mathrm{d}r}_{:=h_n(y)} = 2 \sum_{n=N_l}^{N_u} A_n h_n(y) \; . \tag{5.4}$$

Since the cosine functions $f_n$ are known each integral $h_n$ can be calculated separately. [Pre91]

The method relies on the fact that both terms (5.3) and (5.4) are using the same coefficients $A_n$, so fitting the original detector signal to formula (5.4) yields

Figure 5.2: Set of cosine basis functions for $N_l = 0, N_u = 3$.

the required coefficients $A_n$ to resemble the emissivity $\epsilon$. The fit is performed with the least–squares method

$$\sum_k \left[ h(y_k) - \text{data}(y_k) \right]^2 \to \min$$

where $h$ is the artifical Abel transform (5.4), data refers to the original detector signal and $y_k$ correspond to the points the measurements are taken from. Derivation leads to the following expression that can be interpreted as a matrix equation from which the coefficients $A_n$ can be obtained via matrix inversion. [Pre91]

$$\forall m: \ 2 \sum_{n=N_l}^{N_u} \left( A_n \sum_k h_n(y_k) h_m(y_k) \right) = \sum_k \text{data}(y_k) h_m(y_k)$$

$$\Leftrightarrow \qquad\qquad A_n \cdot B_{nm} = C_m$$

### 5.2.1   Data preparation

A problem of the used experimental setup is that the camera view on the discharge is limited by both its viewing angle and the flange. However the Abel inversion method described above requires to see as much as possible of the discharge.

An attempt to alleviate this problem is done by taking pictures from each side of the discharge and merging them to one big picture by hand. To gain information of both halves of the discharge, the Abel inversion algorithm is

applied on each side whereas the merging edge acts as the separation point. An example of this processing is provided in Fig. 5.3. Despite the best attempts, the two halves are not exactly symmetric in intensity leading to the merging line in the middle to be visible. This is likely caused by the different tilting angles at which the chamber and the plasma emission are collected.


## 5.3   Results

To compare the results of the Abel inversion method with those of the probes, the area of the merged picture corresponding to the probes' position is binned vertically before the Abel inversion is applied. In addition, each pixel is assigned horizontally to the equivalent position relative to the center of the plasma chamber by using the lower plate from the pictures as a point of reference. This leads to line–processed emissivity profiles which is shown for $10\,\mathrm{Pa}$ in Fig. 5.4 which will be discussed in the following. The results for the $3\,\mathrm{Pa}$ and $20\,\mathrm{Pa}$ measurements are displayed later in Fig. 6.6 and Fig. 6.7, respectively, along with the results of the other methods.

In all of the following presented results the expansion limits are set to $N_l = 0$ and $N_u = 16$. The signal–to–noise ratio of the fit to the original data can be adjusted by varying these parameters [Pre91]. No further smoothing as well as no background correction is applied considering heterogeneous wall reflections from the plasma chamber.

Since both sides of the discharge are processed independently, they do not necessarily need to connect at the merging edge which also applies on the Abel inverted data. If both sides would be completely symmetric though, this would not be an issue. At the border regions the fit falls down to zero contrary to the original data. Responsible for this problem is the requirement of the Abel inversion method to have full view on the discharge which is not delivered in the camera pictures. As seen in the figures this also has an impact on the Abel inverted data close to the edges. These observations are both denoted as numerical artifacts.

The Abel inversion algorithm can be used to process the whole picture line–wise. This was done for each measurement and is displayed in Fig. 5.5, 5.6 and 5.7. For higher pressures the discharge appears to be more localized such that less artifacts appear at the edges. Also a sheath near the upper quartz dome is noticeable that seems to keep the plasma away from it. The sheath width decreases with increase of the pressure and, thus, of the plasma density. The sheath occurs most likely due to the electric field generated by the RF antenna. Due to the spiral geometry of the antenna the field intensity is higher in the center region than in the border region yielding the specific shape of the sheath.
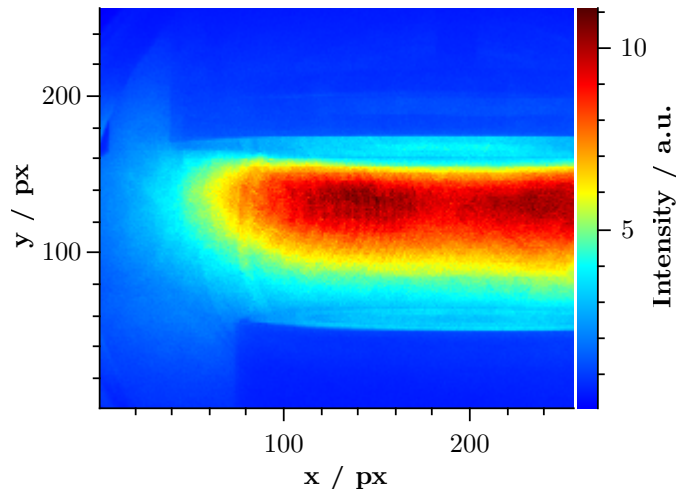
(a) Left side of the discharge.
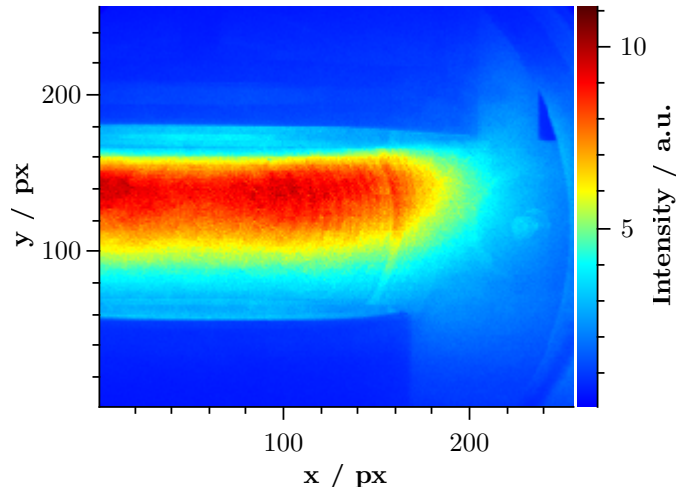


(b) Right side of the discharge.
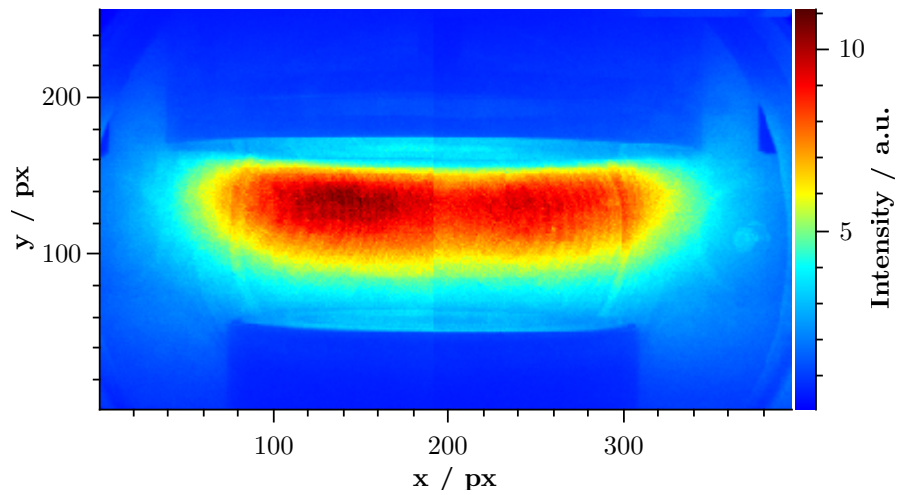


(c) Both pictures (a) and (b) merged.

Figure 5.3: Merging pictures of both halves of the discharge to one picture. Here the discharge is running at 3 Pa.

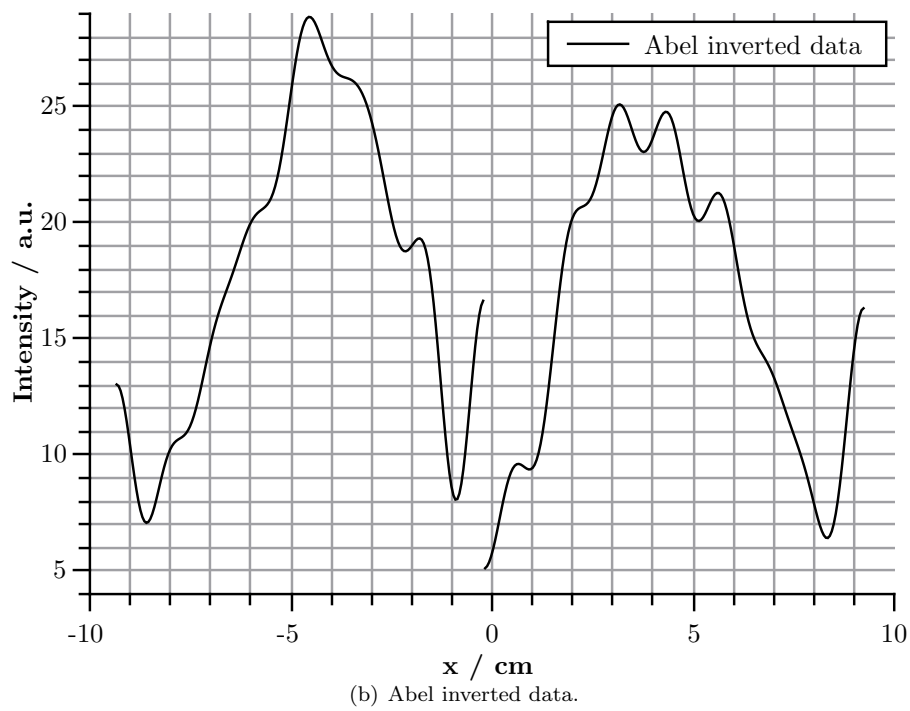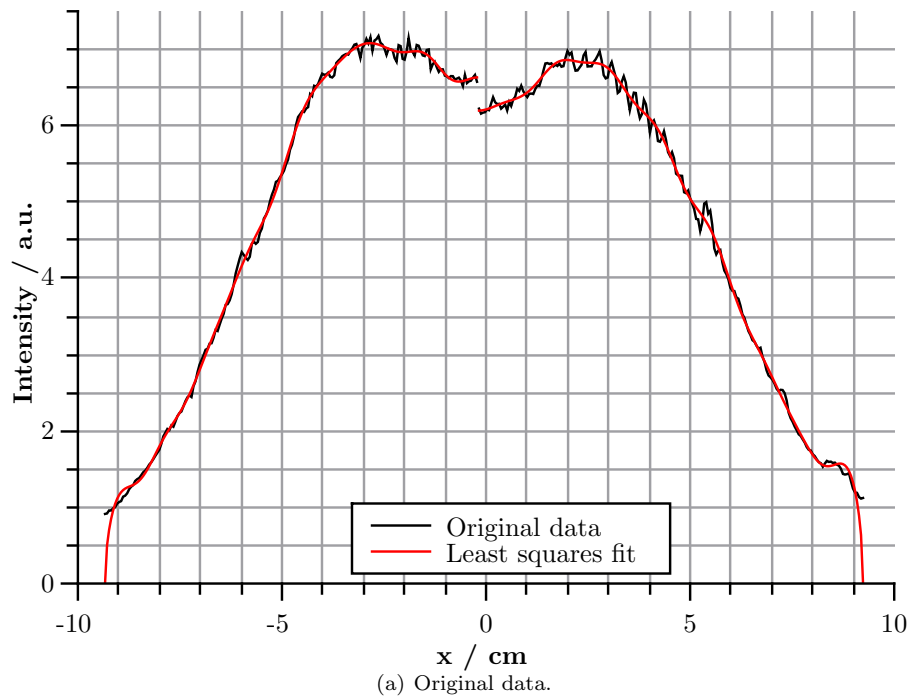(a) Original data.



(b) Abel inverted data.

Figure 5.4: Processed line of the discharge running at 10 Pa corresponding to the vertical position of the probes.
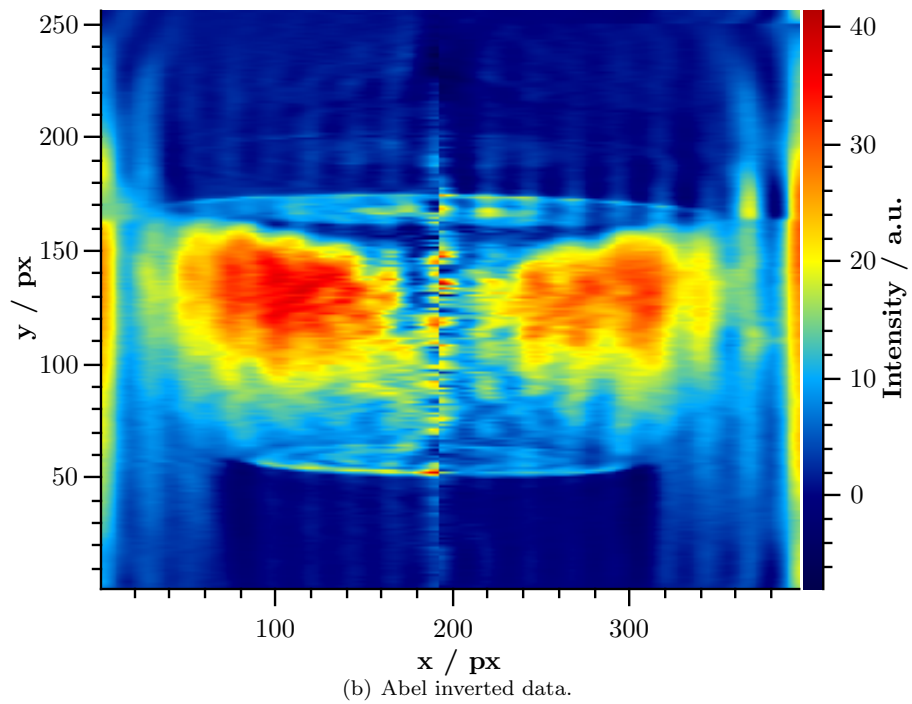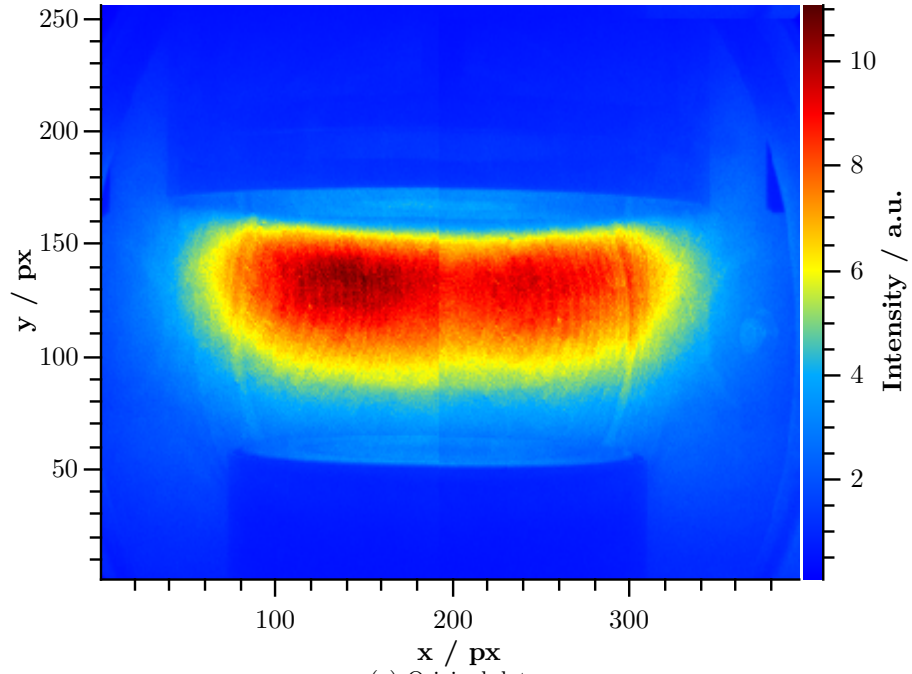
(a) Original data.



(b) Abel inverted data.

Figure 5.5: Fully processed picture of the discharge running at 3 Pa.
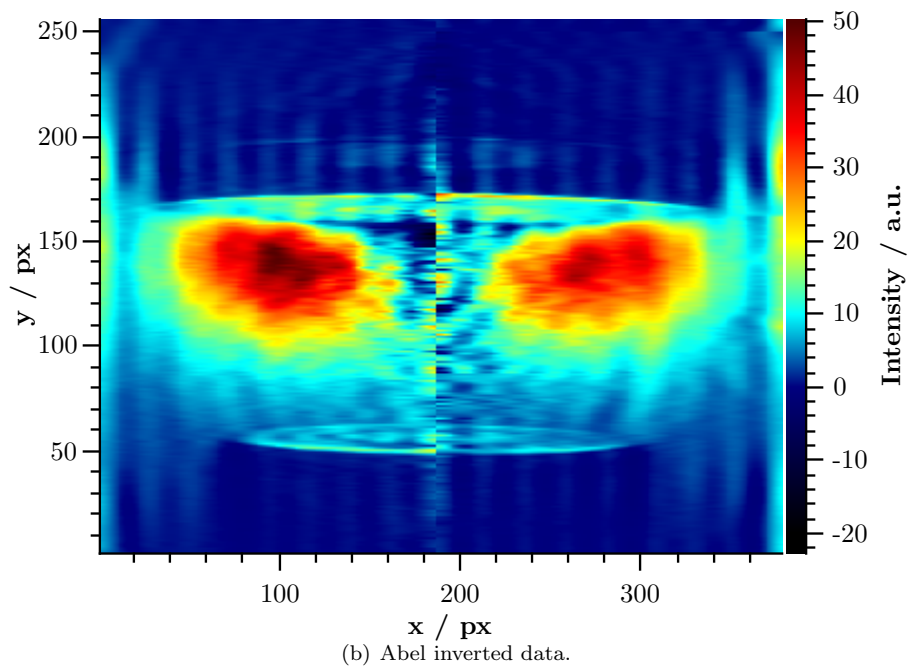
(a) Original data.
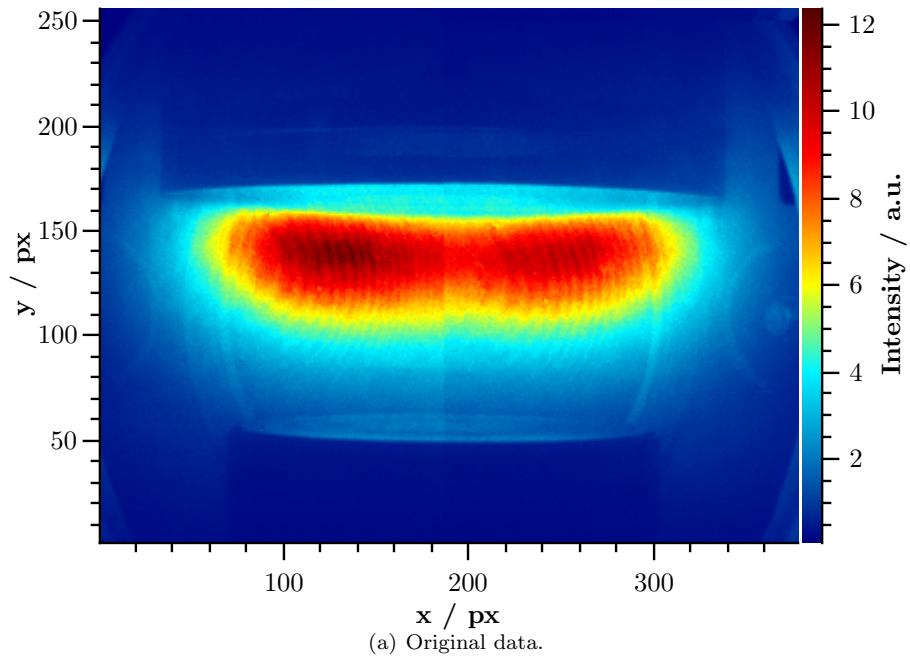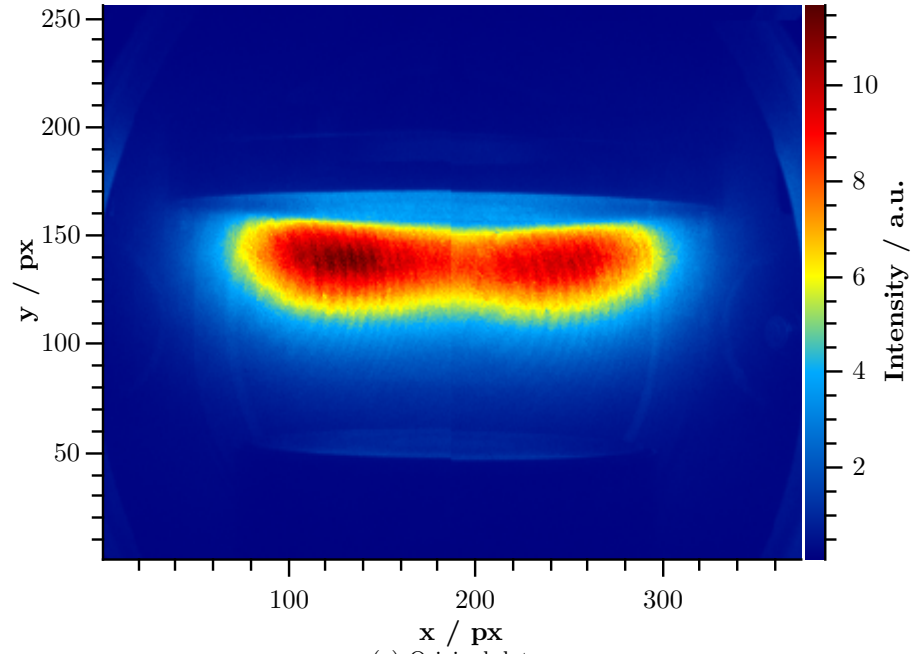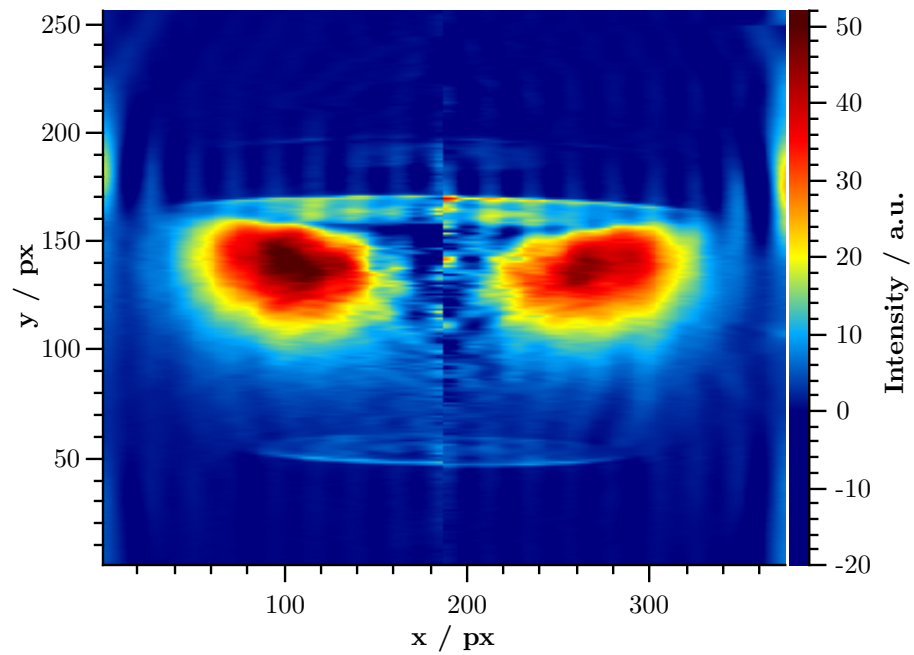

(b) Abel inverted data.

Figure 5.6: Fully processed picture of the discharge running at 10 Pa.

(a) Original data.



(b) Abel inverted data.

Figure 5.7: Fully processed picture of the discharge running at 20 Pa.

# Chapter 6

# Comparision of the results

## 6.1  Langmuir probe measurements

Fig. 6.1 shows the plasma parameters that were calculated with formulas (4.3) and (4.5) and the plasma potential for a discharge at 10 Pa. The electron density is scaled by a factor of $10^{-16}$. As one can see the parameters after the middle of the chamber (-0.2 cm) do not show consistent behavior and are therefore of limited reliability. The most likely explanation is disturbance of the plasma by the probe. The disturbance gets higher when the probe is entered further into the plasma. Assuming that the discharge is symmetrical the plasma parameters are mirrored at the middle of the chamber. So just the measurements when the probe is entered up till the middle (from $x = $ -12.7 cm till -0.2 cm) are used.

The resulting graph is shown in Fig. 6.2. One can see that the electron density is at its highest in the middle of the chamber. To be specific it is at its highest in the area where the coil is. The coil has a diameter of 12 cm and goes from -6 cm to 6 cm. This is to be expected since in the area below the coil the electric field is the highest, so the ionization rate is also high. Outside of the coil area the electron density decreases nearly linearly. This happens because the electrons diffuse out of the plasma and no new electrons are produced by ionization.

The plasma potential follows the shape of the electron density.

The effective temperature has a double peak structure. The peaks are at -4 cm and 4 cm. In the middle of the chamber and at the edges are the minima. This is consistent with the expected distribution of the RF electric field and the locality in the electron heating. The red dots show three different probe positions for which the EEDFs are shown in Fig. 6.3.

One can see that at -9.7 cm the probability for low energy electrons, the maximum of the graph is the highest in comparison to the others, whereas the slope is the steepest. This means that the probability for high energy electrons is very small compared with the other two. For -3.7 cm the probability for low energy electrons is the smallest. But the slope is not so steep, so that the probability for high energy electrons is way higher. Therefore, the mean
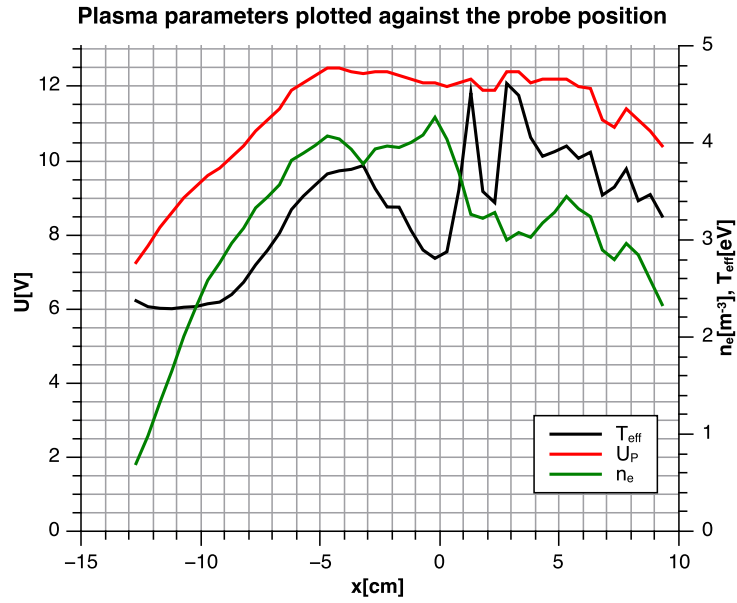
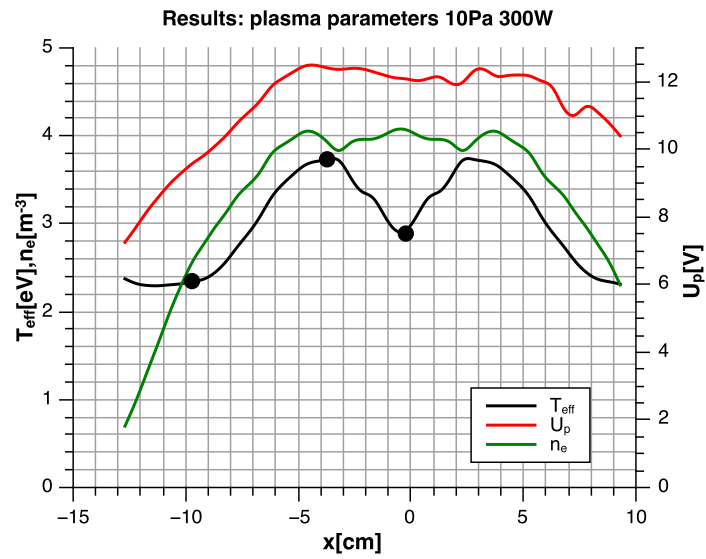Figure 6.1: Measured plasma parameters over probe position at 10 Pa.



Figure 6.2: End results for the plasma parameters at 10 Pa.

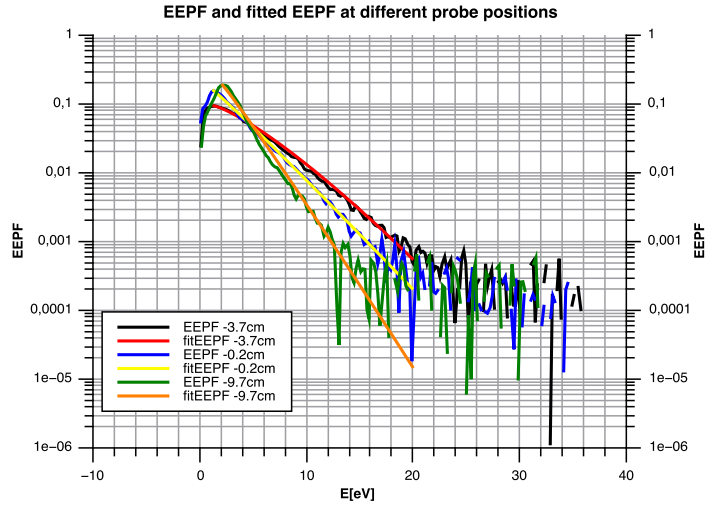**EEPF and fitted EEPF at different probe positions**



Figure 6.3: EEPF for 3 different probe positions marked in Fig. 6.2.

energy and, accordingly, the effective temperature are highest at this position (see fig. 6.2. At -0.2 cm the maximum is a little bit smaller and the steepness is in between of the other two probe positions. So the temperature is a little bit higher than the temperature at -9.7 cm.

For 3 Pa and 20 Pa the plasma parameters show similar behavior, so they are not shown here.

### 6.1.1  Excitation rate and Arrhenius form

In Fig. 6.4 one sees that the Arrhenius form has nearly the same shape as the excitation rate. Only the first two peaks on the right side are higher in the Arrhenius shape. But that could also be because the excitation rate is based on the fitted EEDF whereas the Arrhenius form is based on the effective temperature which is based on the measured EEDF. The green curve shows the Arrhenius form without the electron density. It has the same shape as the excitation rate and the Arrhenius form. So the electron density doesn't shape the rate coefficient but acts as a scaling factor only.

The shape of the Arrhenius form and the excitation rate is nearly the same although the shape of the Arrhenius form is given by the mean energy whereas the shape of the excitation rate is given by the tail of the EEDF and so by the high energy electrons. This is a consequence of the nearly Maxwellian shape of the EEDF.
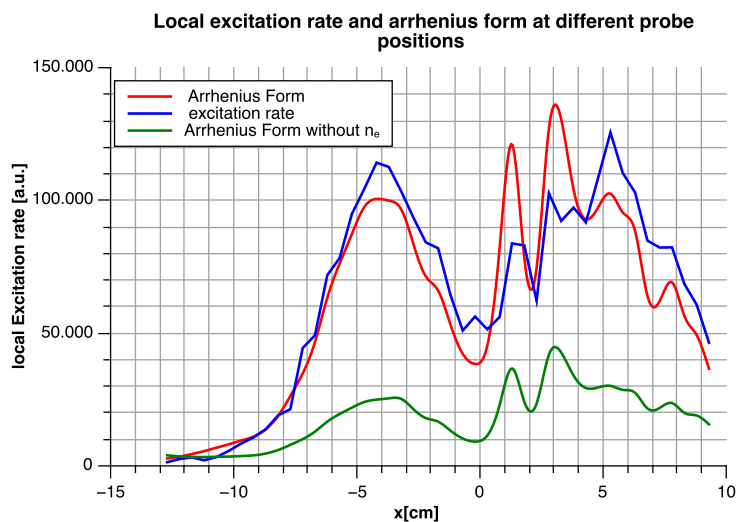
Figure 6.4: Excitation rate and Arrhenius form at 10 Pa.

## 6.2   Comparison of local emissivity profiles

Fig. 6.5 shows the local emissivities for our three methods. We scaled the local emissivity so that the highest value obtained with all three methods is nearly the same. So the absolute value of the emissivity obtained with one method can not be compared with the emissivity obtained with another. But the shapes of the curves are comparable. The two probes where entered at the position -12.5 cm. The $x$–position for the Abel inversion was calculated by knowing the exact size of the electrodes.

As we can see the shape of the curves is the same for all three methods. We find two peaks at -4 cm and 4 cm. At 0 cm we find a minimum for all curves similarly to the already shown behavior of the electron temperature. The position of the maximum peaks makes sense, because they are at $\frac{2}{3}$ of the coil radius where the electric field is at its highest. So at this point the electrons have their highest energy. Because of that the excitation and the emission rates are also at their maximum. As Fig. 6.2 shows, the electron density is relatively flat in the central region. Therefore, the excitation is determined mostly by variation of the electron energy. Under the assumption of local energy gain and heating, an assumption which is well justified due to the molecular nature of the used gas, the electron energy should follow the profile of the heating RF filed. As already discussed, this is indeed the case.

The values from the optical probe (red curve) at the edges are less reliable. So we ignore the behavior of the optical probe curve at the edges in the discussions. The behavior is because of our used derivation method. The first peak at -8 cm is a mechanical artifact of the probe. We find it in every measurement for all pressures [DCLC10].
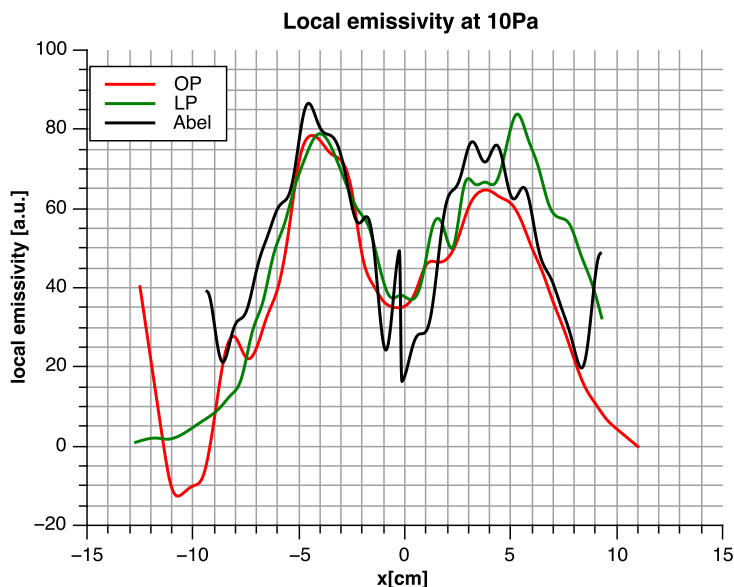
Figure 6.5: Local emissivity obtained with all three methods at 10 Pa : Op–optical probe, LP–Langmuir probe and Abel–Abel inversion.

For the Abel inversion (black curve), the rising at the edges and the center is a result of numerical artifacts as described in chapter 5.

For the Langmuir probe the shape of the second peak is not trustworthy, because its too different in comparison to the other two techniques. The problem with the Langmuir probe is that the further it is entered into the plasma, the more the plasma is disturbed. We see that for the Abel inversion the height and width of the two peaks is nearly the same. For the optical probe we can see that the first peak is higher but more narrow than the second peak. We assume that this is because of disturbances in the plasma caused by the probe.

Fig. 6.6 shows the local emissivity at 3 Pa. The shape of the curve for all three methods is the same. This time the second peak is smaller for all three methods and the shape of the Langmuir probe fits better to the other two methods. Because of this we think that for 3 Pa the disturbances in the plasma caused by the probe are smaller.

For 20 Pa (see Fig. 6.7) Abel inversion and the optical probe have the same curve shape. The two peaks are even symmetrical for both methods. The Langmuir probe measurement is not trustworthy because it differs too much from the other two methods. That is because for 20 Pa the discharge was smaller and was not positioned in the center of the cell, but more orientated towards the coil. So the Langmuir probe measured the plasma at the edges and the disturbance through the probe is bigger. However, despite the differences the overall shapes of all three methods show rather reasonable agreement under the conditions of the experiment.
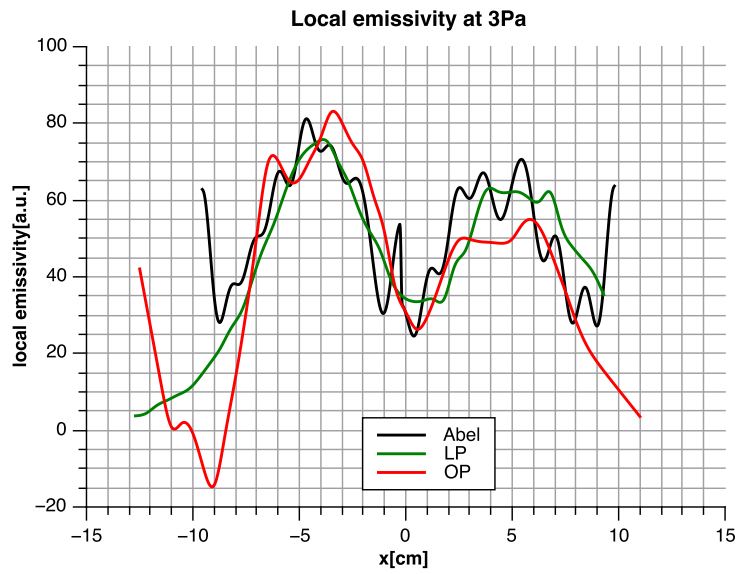
Figure 6.6: Local emissivity obtained with all three methods at 3 Pa : Op–optical probe, LP–Langmuir probe and Abel–Abel inversion.
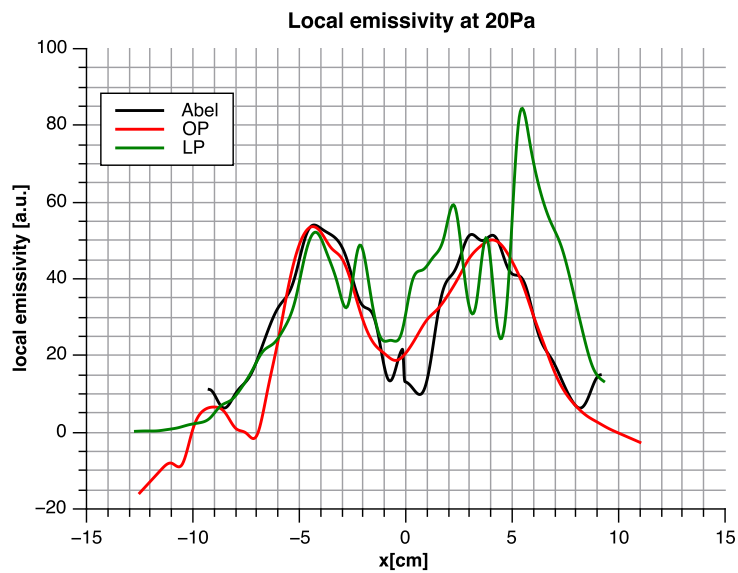


Figure 6.7: Local emissivity obtained with all three methods at 20 Pa : Op–optical probe, LP–Langmuir probe and Abel–Abel inversion.

## 6.3  Emission profiles for various pressures

Fig. 6.8 shows the local emissivity obtained with the optical probe for 3 10 and 20 Pa. We can see that for rising pressures the peaks get more distinct and the peak value rises. Also the second peak gets more of the shape of the first peak the higher the pressure gets. So for 20 Pa a symmetrical local emissivity profile is obtained.

Fig. 6.9 shows the Abel inversion emission profiles for various pressures. For the Abel inversion the peak value diminishes with rising pressure. But we can see that the peaks get more distinct for rising pressures which is noticeable by the width of the peaks. For rising pressure the width gets smaller.
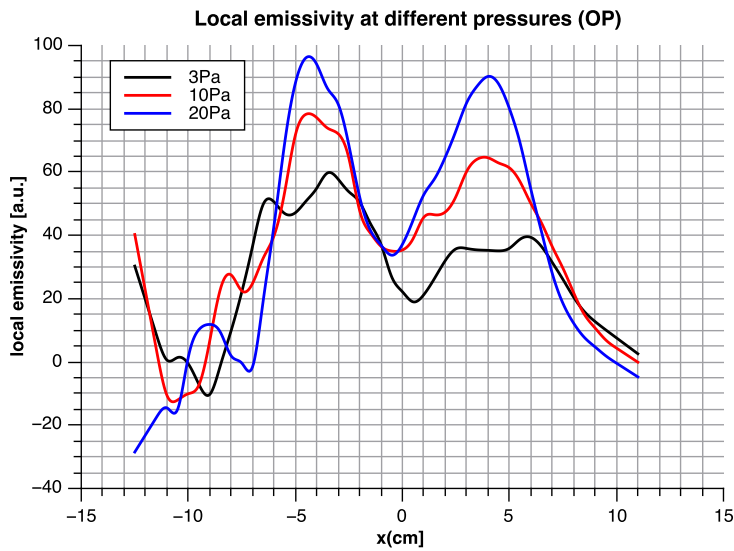


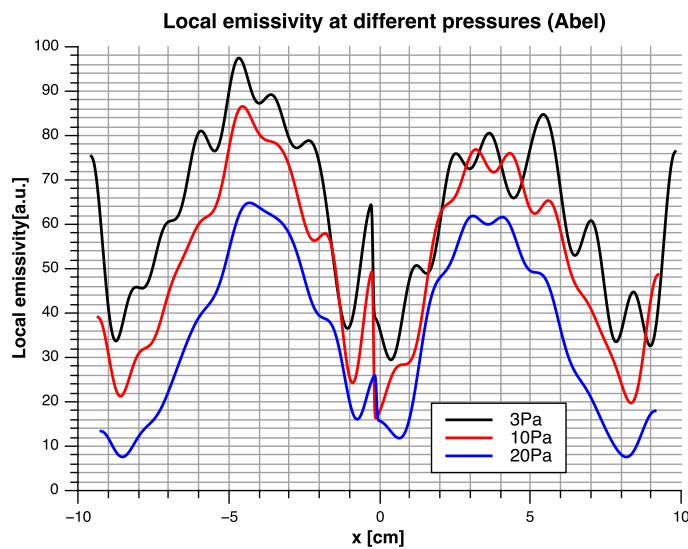Figure 6.8: Local emissivity obtained with the optical probe at 3,10,20 Pa.



Figure 6.9: Local emissivity obtained with the Abel inversion at 3,10,20 Pa.

# Chapter 7

# Conclusions

As described in chapter 6 all methods provide similar emissivity profiles and, therefore, the results are in good agreement. In the following a short rating of each method based on experience from this experiment is provided.

In terms of difficulties analyzing the detector signal, the optical probe is the easiest method since only the derivation of the detector signal is required. However, due to the small solid angle of the detected light, a high signal intensity is needed to detect anything.

Once the program for Abel inversion is written, it is the fastest method. Just take a picture of the discharge and let the algorithm do the work. Attention needs to be paid on the numerical artifacts in both border and axial region which occur in the proposed method.

The Langmuir probe gives most information out of the plasma. In the course of chapter 4 many plasma parameters were derived, for example electron temperature, electron density, plasma potential etc., but to obtain the emission profile, additional data is needed, namely the excitation cross section. Also caution is required on the high signal–to–noise–ratio of the EEPF for high energies. Another major drawback is that the probe itself disturbs the plasma such that the data in the second half of the plasma is not reliable.

There are many different ways to obtain the spatially resolved emission profile of a plasma each with their own benefits and drawbacks that have to be taken into account when planning an experiment. However, since all of the methods deliver in the end the same information, the particular choice of diagnostics depends ultimately on the available equipment and the personal liking of the experimentalist.

# References

[DCLC10]  Beilei Du, Yusuf Celik, Dirk Luggenhölscher, and Uwe Czarnetzki. A novel probe for spatially resolved emission spectroscopy in plasmas. *Plasma Sources Science and Technology*, 19(4):045008, June 2010. `doi:10.1088/0963-0252/19/4/045008`.

[Dru30]  M. J. Druyvesteyn. Der Niedervoltbogen. *Zeitschrift für Physik*, 64(11–12):781–798, September 1930. `doi:10.1007/BF01773007`.

[JRS03]  R.K. Janev, D. Reiter, and U. Samm. Collision processes in low–temperature hydrogen plasmas. Berichte des Forschungszentrums Jülich JUEL-4105, Institut für Plasmaphysik (IPP), Forschungszentrum Jülich, 2003. URL: `http://hdl.handle.net/2128/249` [cited 2015-03-20].

[Pre91]  Georg Pretzler. A new method for numerical Abel–inversion. *Zeitschrift für Naturforschung A*, 46a:639–641, January 1991. URL: `http://zfn.mpdl.mpg.de/data/Reihe_A/46/ZNA-1991-46a-0639.pdf` [cited 2015-03-20].

[SG64]  Abraham Savitzky and Marcel J. E. Golay. Smoothing and differentiation of data by simplified least squares procedures. *Analytical Chemistry*, 36:1627–1639, July 1964. `doi:10.1021/ac60214a047`.

[Tho]  M. Thomson. Abelinversion. URL: `http://www.ilp.physik.uni-essen.de/doebele/projekte/Archiv/abelinversion/abelinv.html` [cited 2015-03-20].